coatings

MDPI

*Article*

# Oxidation and Mechanical Behavior of Cr-Coated Laser Beam Welds Made from E110 Zirconium Alloy

**E. B. Kashkarov *, K. S. Gusev, D. A. Ashikhmin, A. V. Abdulmenova and D. V. Sidelev**

School of Nuclear Science and Engineering, Tomsk Polytechnic University, 30 Lenina Av., Tomsk 634050, Russia
* Correspondence: ebk@tpu.ru; Tel.: +7-38-2270-1777 (ext. 1562)

**Abstract:** This article describes the oxidation resistance of laser beam welds made from E110 zirconium alloy with a chromium coating obtained using multi-cathode magnetron sputtering. Oxidation tests of the welded Zr alloy without and with Cr coating were performed in an air atmosphere at 1100 °C for 2–90 min. Then, analysis of their cross-section microstructure in different regions (weld, heat-affected, and bulk zones) was done using optical microscopy. Hardness measurements and three-point bending tests demonstrated the hardening of the Cr-coated welded Zr alloy after the oxidation that is discussed in the article. Brittle fracture behavior was observed for uncoated Zr weld even after a short period of high-temperature oxidation.

**Keywords:** laser beam welding; zirconium alloys; chromium coating; high-temperature oxidation; magnetron sputtering; three-point bending test



**Citation:** Kashkarov, E.B.; Gusev, K.S.; Ashikhmin, D.A.; Abdulmenova, A.V.; Sidelev, D.V. Oxidation and Mechanical Behavior of Cr-Coated Laser Beam Welds Made from E110 Zirconium Alloy. *Coatings* **2022**, *12*, 1623. https://doi.org/10.3390/coatings12111623

Academic Editor: Angela De Bonis

Received: 30 September 2022
Accepted: 24 October 2022
Published: 26 October 2022



## 1. Introduction

Zirconium alloys with Sn or Nb dopants are used as the base structural material of fuel assemblies for light water reactors (LWRs) because of their relevant mechanical properties, good radiation and corrosion resistance under normal operation conditions (~360 °C and 18.6 MPa) [1]. However, possible accidents in LWRs can result in a temperature ramp of fuel assemblies leading to their crucial oxidation and hydrogen embrittlement since Zr alloys can fast interact with a water steam. It can cause failures of Zr alloy fuel claddings and/or spacer grits of nuclear assemblies. To date, several ongoing studies of candidate structural material for LWRs are still being performed [2–7]. The main attention is focused on their oxidation resistance under accidental conditions, e.g., at a loss of coolant accident as it occurred in the Fukushima nuclear power plant [8–10]. A new type of nuclear fuel, a so-called accident tolerant fuel (ATF) should have enhanced resistance to high-temperature corrosion in a water steam. The short-term strategy of ATF development consists of the deposition of a protective coating on the outer surface of nuclear fuel assembly made from Zr alloys. Based on a lot of published materials [11–13], chromium is suggested as a relevant candidate material as a protective coating for the above-mentioned task. However, special attention should be devoted to the protection of elements having welded joints, as welding is applied to produce spacer grits and/or to weld ends to fuel cladding tubes [14]. Despite the fact that a lot of experiments have been done to determine relevant parameters of Zr alloy welding [15–18], excluding the formation of cracks, uptake of gaseous species from the atmosphere, and saving mechanical properties, structural properties of welded Zr alloys will differ from bulk. It is well known [19] that welded material has three typical regions such as weld (WZ), heat-affected (HAZ), and bulk zones. Vandegrift J. et al. showed accelerated oxidation of Zry-3, Zry-4, and Zr–1Nb tubes in WZ as larger grains were found in comparison with HAZ and bulk regions [20]. Fast solidification of welded Zr alloys can result in forming columnar microstructure and saturation of dopants in the β-Zr phase leading to decrease corrosion resistance of welds [15,21]. The corrosion behavior of laser beam welded joints of Zr alloys can be improved by applying a post-treatment annealing as

saturated Nb in β-Zr phase precipitated as second phase particles [16,18]. Despite the latter, the resistance of Zr alloy welds to high-temperature oxidation is so low that the deposition of protective coating on the weld surface should be applied.

The influence of Cr coating deposition on oxidation behavior (at 1100 °C) of resistance upset (RUW) and laser beam welds (LBW) from Zr alloy was earlier studied in [22,23], which found that the microstructure of welded alloy did not change under Cr coating deposition by magnetron sputtering and high-temperature oxidation of Zr alloy welds can be prevented applying 8 μm-thick Cr coating. However, high-temperature tests had a short duration of the isothermal oxidation stage; it was equal to 2–10 and 2–30 min for LBW and RUW samples, respectively. As the Cr coating deposition is considered as the approach to induce additional "coping" time before failure of ATF Zr alloy assembly in a temperature range up to 1200–1300 °C [11], corrosion resistance of Cr-coated welds should be determined for longer oxidation duration. Moreover, the mechanical properties of welded Zr alloy after high-temperature oxidation have to be estimated as it is important for saving the integrity of nuclear fuel assemblies under accidental conditions.

Thus, this study aims to determine the oxidation resistance of Cr-coated Zr alloy welds and their mechanical properties after long-term high-temperature oxidation. Samples of laser beam welds produced from E110 zirconium alloy were selected in this study.

## 2. Experimental Details

### *2.1. Sample Preparation*

Laser beam welds from the E110 (0.9–1.1 wt% Nb, 0.06–0.1 wt% O, and Zr balance) zirconium alloy was manufactured by PJSC "Novosibirsk Chemical Concentrates Plant" (NCCP, Rosatom, Novosibirsk, Russia). The obtained LBW samples were divided into two series. The first series comprised the LBW samples in the initial state without any post-treatment procedures after welding. The second series of samples was coated with a chromium coating. Prior to the coating process, the samples were treated in an ultrasonic bath with acetone (20 min) and then blasted with dry air for two min. After it, the LBW E110 alloy samples were kept in special substrate holders in such case that some surface area of the samples remained uncoated after the deposition process (the uncoated area was equal to ~0.25 $cm^2$). Substrate holders were installed in the planetary rotated table for uniform surface treatment of the samples. Ion bombardment by Ar ions was applied for etching the surface of the samples. The following parameters of ion etching were used: Ar pressure—0.2 Pa, ion current—35 mA, accelerated voltage—2.5 kV, etching time—30 min.

Chromium coating deposition was done using the vacuum plasma installation equipped with a multi-cathode magnetron sputtering system with Cr (99.95%, Ø90 mm) targets. Its detailed description is presented in [24]. Deposition parameters of Cr coating on the LBW E110 alloy samples (Table 1) were selected based on previous results in refs [22,23]. The thickness of the Cr coating was equal to 14.4 μm.

**Table 1.** Deposition parameters of Cr coating.

| $P$, Pa | $Q_t$, W/$cm^2$ | $f$, kHz | $d$, % | $U_b$, V | $j_s$, mA/$cm^2$ | $t$, min | $h$, μm |
|---|---|---|---|---|---|---|---|
| 0.3 | 39 | 50 | 80 | −100 | 24 | 210 | 14.4 |

Note: $P$—operation pressure; $Q_t$—target power density; $f$—pulse frequency; $d$—duty cycle; $U_b$—substrate bias; $j_s$—ion current density to a substrate; $t$—deposition time; $h$—coating thickness.

### *2.2. High-Temperature Oxidation and Sample Characterization*

The experimental samples were oxidized in an air atmosphere (humidity—70%) using a high-temperature furnace ATS 3210 (Applied Test Systems Inc., Butler, PA, USA). Initially, the samples were kept in a cold furnace (~25 °C) and then they were heated up to 1100 °C at a rate of ~25 °C/min. The duration of the isothermal stage was equal to 2, 10, 30, 45, and 90 min. After this, the samples were cooled to room temperature. The weight gain of the samples was determined by an analytical balance Sartorius CP124 S.

A cross-section microstructure of the samples was studied using an optical microscope AXIOVERT 200MAT. Preliminary, a surface of cross-sections of the samples was etched in a solution of 5 vol.% HF + 45 vol.% $HNO_3$ + 50 vol.% $H_2O$ at room temperature.

The hardness of the samples was determined by a hardness tester Pruftechnik KB-30S equipped with a Vickers indenter. The indenter load was 50 g. Hardness measurements were performed in three different zones (WZ, HAZ, and bulk), at least 20 indentations were done in each zone.

Three-point bending test was performed using an installation Gotech Al-7000M with one impact and two supporting rollers. The initial load was 0.1 N to start the experiment, experimental data (load and displacement) was recorded with a frequency of 124 Hz. The bending tests were done in the displacement control mode with a loading rate of 0.5 mm/min according to the E290 ASTM standard. The distance between two supporting rollers was equal to 22 mm, while the center of the LBW samples (WZ) was set on the impact roller. Cross-section of the LBW E110 alloy samples was also studied after the bending test using a scanning electron microscopy (SEM, JEOL JSM 7500F) with an energy dispersive X-ray spectroscopy (EDS) attachment for elemental analysis. This analysis was carried out using the equipment of the CSU NMNT TPU, supported by the RF MES project #075-15-2021-710. Note that the samples were polished to expose their cross-sections after the bending tests.

## 3. Results

### *3.1. Weight Gain of the Samples*

The dependencies of the weight gain of uncoated and Cr-coated LBW samples on oxidation time are shown in Figure 1. The weight gain of uncoated samples is significantly higher than that of Cr-coated samples. The crucial role of Cr coating on weight gain of Zr alloys under high-temperature oxidation was earlier observed in [11,25]. Thus, the deposition of Cr coatings increases the oxidation resistance of LBW Zr alloy samples by 5.7 and 6.6 times after 2 and 10 min oxidation, respectively.

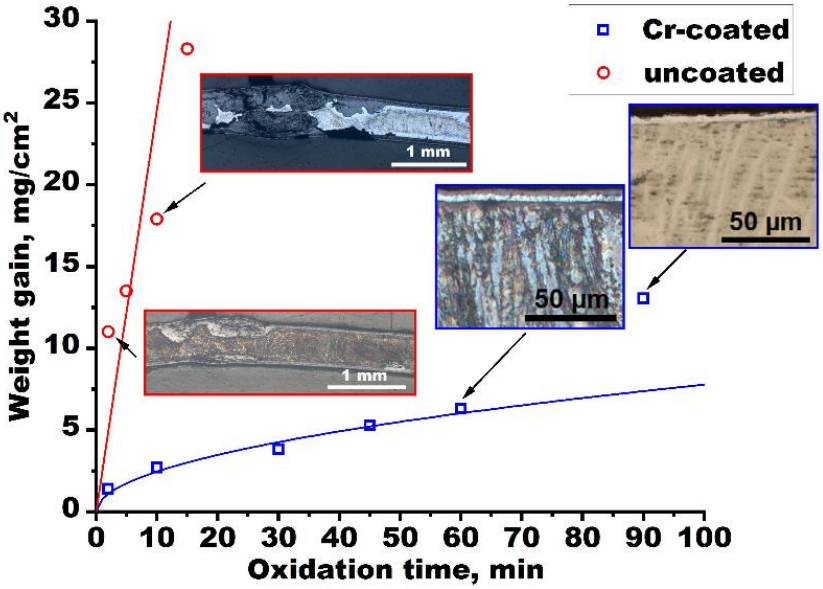


**Figure 1.** Dependencies of the weight gain of uncoated and Cr-coated LBW E110 alloy samples on oxidation time. Insets show optical images of the cross-section microstructure of the samples in general (uncoated LBW) and in a surface region (for Cr-coated samples).

The oxidation kinetics of uncoated LBW samples has a nearly linear dependence, which coincides well with data from other works that have studied high-temperature oxidation of Zr alloys in a nitrogen-containing atmosphere [26,27]. According to optical

images (Figure 1), the thick oxide layer (~180–250 μm) is found in the uncoated LBW sample even after 2 min oxidation. Oxidation over a full thickness of the LBW sample is observed after the oxidation test for 10 min. The Cr-coated samples demonstrate parabolic oxidation kinetics of up to 60 min. Such dependence is typical for the oxidation of metals under diffusion-controlled growth of the protective oxide layer on their surface [11,28,29]. However, there is a significant increase in the weight gain for the Cr-coated sample from 60 to 90 min of oxidation (6.3→13 mg/cm$^2$), which does not correspond to the parabolic dependence. The cross-section optical images of the samples in a surface region after 60 and 90 min oxidation show that both samples have an outer protective scale and no oxidation of the LBW alloy. So, such an increase in the weight gain causes by the strong oxidation of the uncoated area of the Cr-coated LBW sample.

### *3.2. Cross-Section Microstructure after Oxidation*

LBW samples before HT oxidation had a typical microstructure in each zone (WZ, HAZ, and bulk). The cross-section microstructure of uncoated samples after high-temperature oxidation was previously studied and presented in the previous paper [23]. In this study, a detailed microstructure analysis was performed for Cr-coated LBW E110 alloy samples after their oxidation for a longer oxidation time (up to 90 min). Figure 2 demonstrates the typical protective scale for the Cr-coated LBW E110 alloy oxidized for 90 min. Due to oxidation, an outer $Cr_2O_3$ layer was formed on the surface of the LBW sample that can prevent further oxygen diffusion into the depth. Then, residual Cr and interdiffusion Cr-Zr layers were presented beneath the outer oxide scale. Based on the obtained data, no meaningful difference in layer thicknesses was found for Cr-coated LBW E110 alloy samples in WZ, HAZ, and bulk zones.

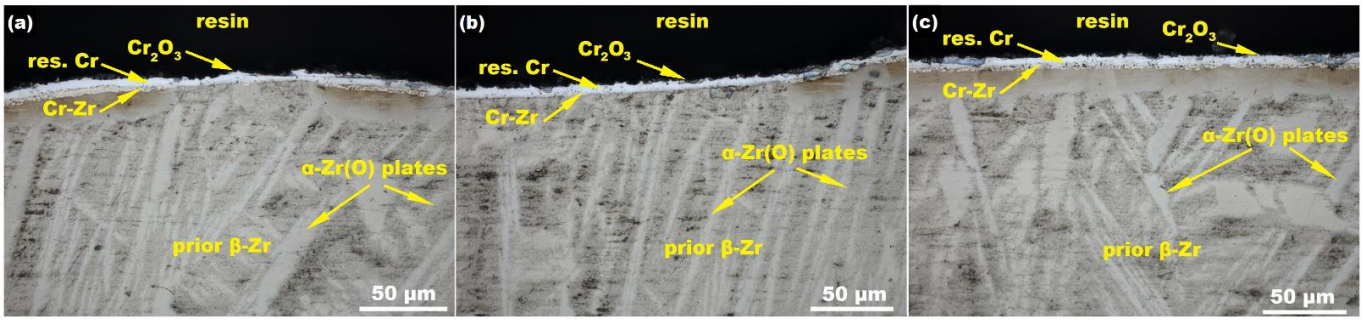


**Figure 2.** OM images of the cross-section microstructure of the Cr-coated LBW sample after 90 min oxidation in a surface region of WZ (**a**), HAZ (**b**), and bulk (**c**) zones.

Figure 3 shows the optical images (OM) of the cross-section microstructure of the Cr-coated LBW E110 alloy for each zone depending on oxidation time. After oxidation, a Widmanstetten microstructure consisting of α-Zr and/or α-Zr(O) plates embedded in primary β-Zr grains was formed in each zone. At up to 30 min oxidation, the microstructure of WZ and HAZ is similar to the microstructure of the initial LBW samples before oxidation, where α-Zr plates formed as a result of fast cooling from β-Zr phase during laser welding [19]. At longer oxidation, the formation of α-Zr(O) plates inside the LBW alloy was observed. The growth of these plates is caused by the diffusion of oxygen through the Cr coating and its dissolution in the β-Zr phase with subsequent stabilization of the α phase. The α-Zr(O) plates are interlaced between each other and mainly oriented transversely to the sample surface. The average thickness of α-Zr(O) plates increases from 3 to 25 μm as the oxidation time increases from 30 to 90 min, respectively.

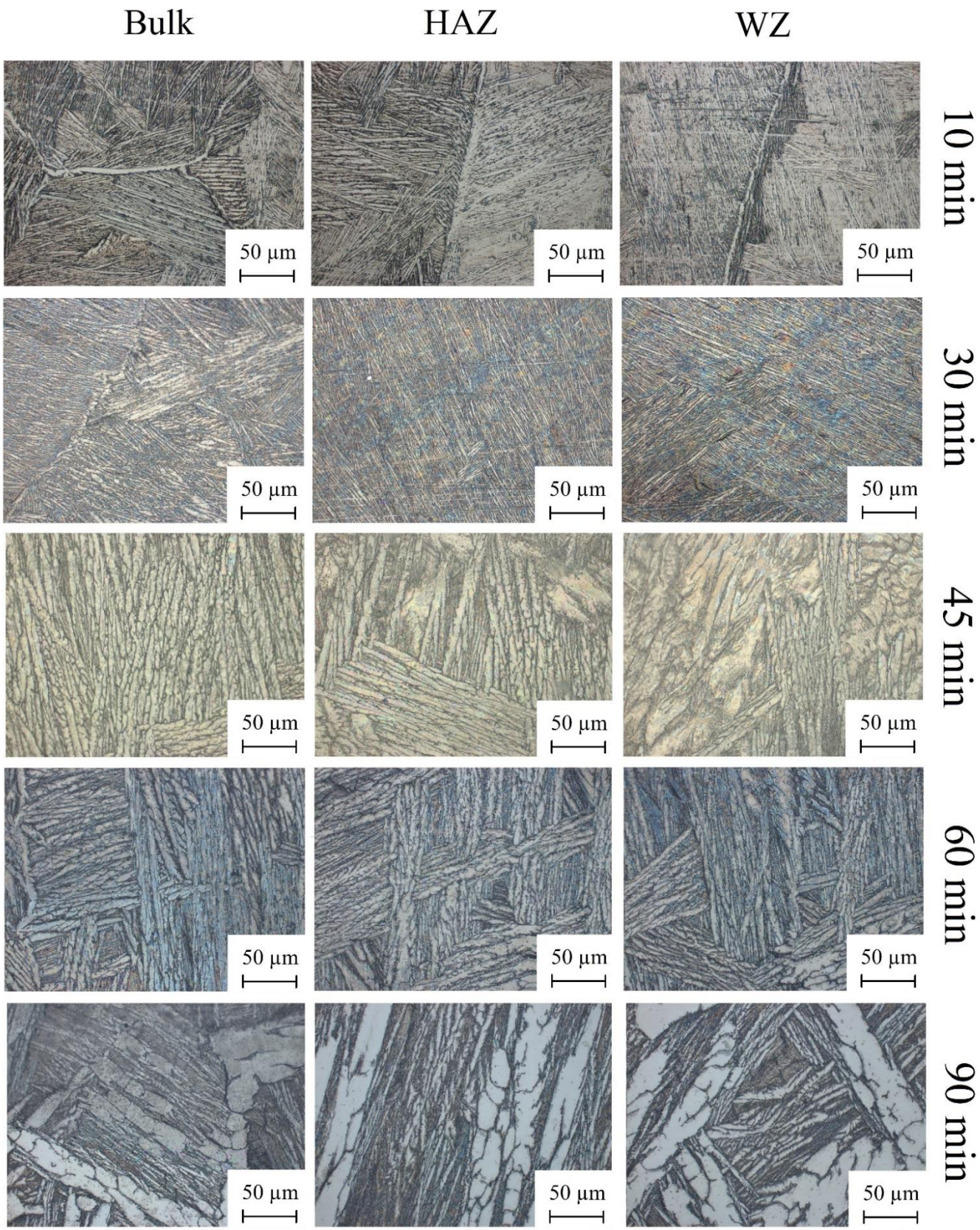


**Figure 3.** OM images of the cross-section microstructure of Cr-coated LBW samples after air oxidation for 10–90 min in WZ, HAZ, and bulk zones.

### *3.3. Hardness of LBW E110 Alloy*

Oxidation has a strong influence on the hardness of the uncoated LBW sample. The increase in hardness in a surface region up to ~1200 HV was found even after a 2 min test due to forming $ZrO_2$ outer layer, which is shown in Figure 1. The hardness beneath the $ZrO_2$ layer decreased from 1200 to 450 HV, when indentations were done in the direction of the internal part of the uncoated LBW E110 alloy [23]. Due to lower oxygen content, the average hardness beneath the $ZrO_2$ layer was equal to ~365 and 350 HV for HAZ and bulk zone, respectively. After 10 min oxidation, WZ and HAZ consisted of brittle $ZrO_2$, so their hardness was not measured due to the poor integrity of samples under indentations [23].

The opposite behavior of hardness was found for Cr-coated LBW samples. Figure 4 presents dependencies between the hardness of Cr-coated samples and oxidation time for different zones (WZ, HAZ, and bulk). The obtained data indicate no significant changes in the hardness up to 30 min oxidation and then, for longer oxidation time, hardness increases. It is well seen that the hardness in WZ, HAZ, and bulk zones increases from 220, 230, and 200 to 370, 350, and 315 HV, respectively. Hardening of the Cr-coated LBW samples is mainly caused by the formation and growth of the oxygen-stabilized α-Zr(O) plates which can have 894–974 HV hardness [30]. These results are well correlated with the cross-section microstructure data (Figure 3). Moreover, it is also found that the hardness in the bulk increases slowly than in WZ and HAZ that is caused by lower thickness of α-Zr(O) plates (~17 μm in bulk zone).

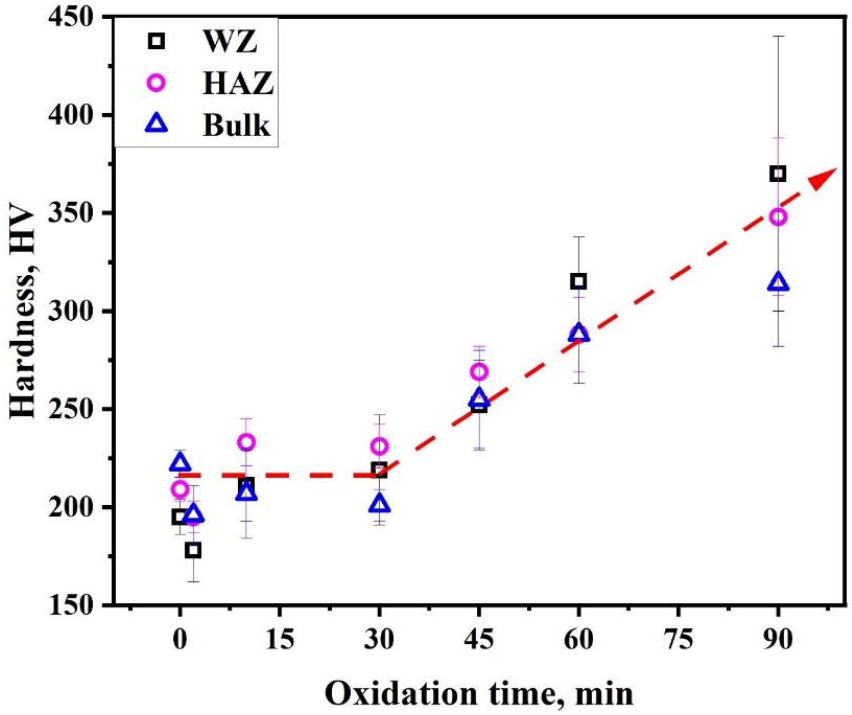


**Figure 4.** Hardness in different zones of Cr-coated LBW E110 alloy samples as a function of oxidation time.

### *3.4. Bending Test*

As LBW E110 alloy samples were hardening under high-temperature oxidation, the bending test was done for both uncoated and Cr-coated samples; then the load-displacement curves were plotted in Figure 5. The bending tests could not be performed for the Cr-coated LBW samples after 60 and 90 min oxidation due to their critical oxidation in the uncoated zone.

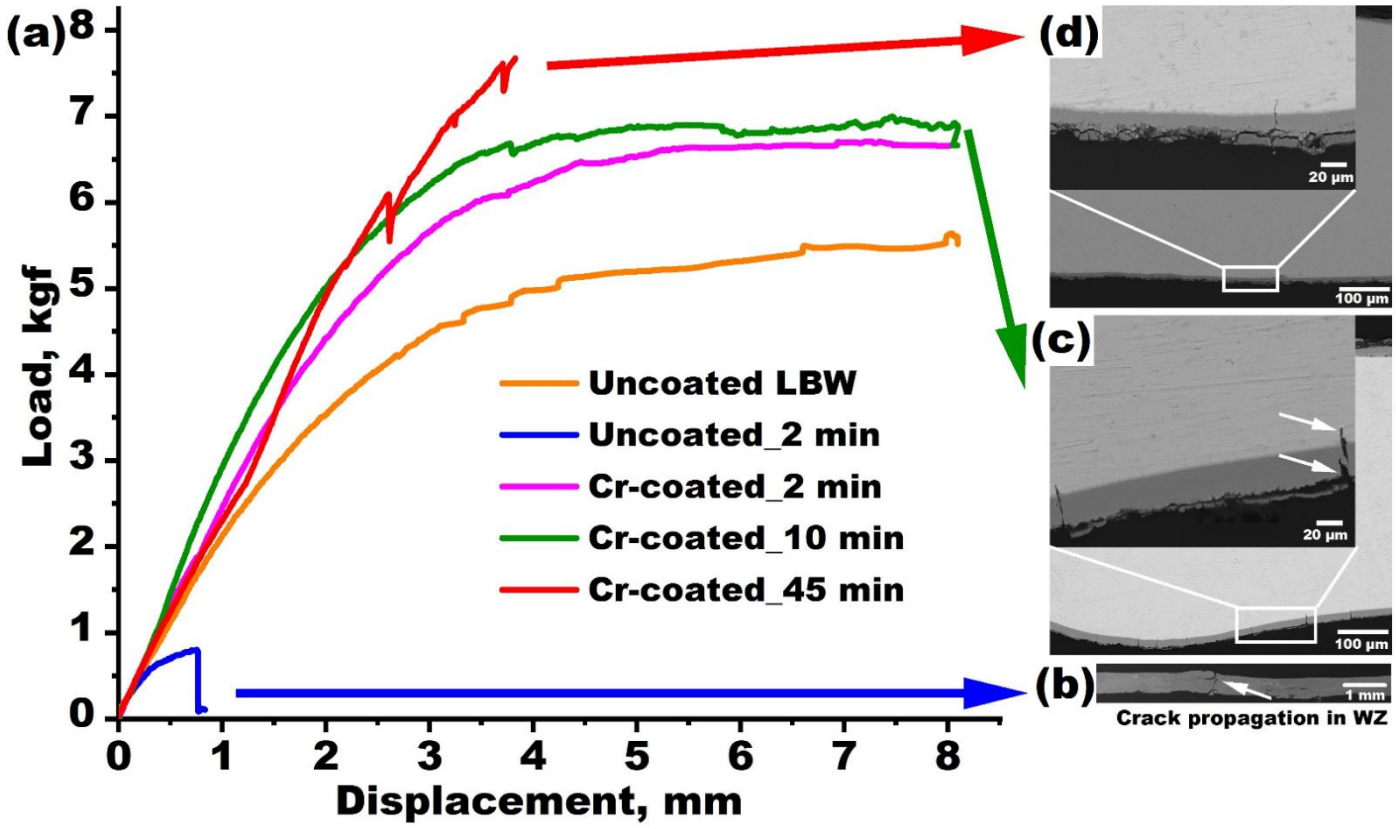


**Figure 5.** Load-displacement curves for uncoated and Cr-coated LBW E110 alloy samples (**a**). Insets show cross-section microstructure SEM images of the samples in WZ after bending tests: (**b**)—uncoated LBW after 2 min oxidation; (**c**)—Cr-coated LBW after 10 min oxidation; (**d**)—Cr-coated LBW after 45 min oxidation.

Prior to the oxidation tests, the uncoated LBW alloy had typical deformation behavior for ductile materials. The transition from elastic to plastic deformation occurred at ~2.5 kgf. The oxidation of the uncoated LBW E110 alloy for 2 min results in their failure even at a displacement of 0.76 mm (load ~0.77 kfg). The sharp drop of load during the bending test was caused by the cracking of the sample in WZ, as is seen from the cross-section SEM image.

The Cr-coated LBW samples after oxidation for 2, 10, and 45 min have load-displacement curves with a typical shape for ductile materials. However, the slope of the curves at the elastic strain region became higher as the oxidation time of the samples was increased from 2 to 45 min. It indicates hardening and increases in the elastic modulus of the samples after longer oxidation tests. The small load drops during the bending tests indicated the initiation and propagation of cracks. Indeed, cross-section microstructure SEM images of the samples after 10 and 45 min oxidation revealed cracking in a surface region. The fracture mechanism of oxidized Cr-coated Zr alloy was earlier determined by an in situ bending test [31,32]. Cracks can be initiated from the surface and Cr/Zr interface since harder outer $Cr_2O_3$ scale and Cr-Zr interlayer formed due to chromium oxidation and Cr-Zr interdiffusion, respectively (Figure 6). Then, cracks can propagate through the residual Cr layer into the LBW alloy up to a depth of 2–10 μm. Interfacial cracks between $Cr_2O_3$ and residual Cr layers are clearly seen in Figure 6. It is most likely that they were formed under the polishing procedure of the samples after the bending tests.

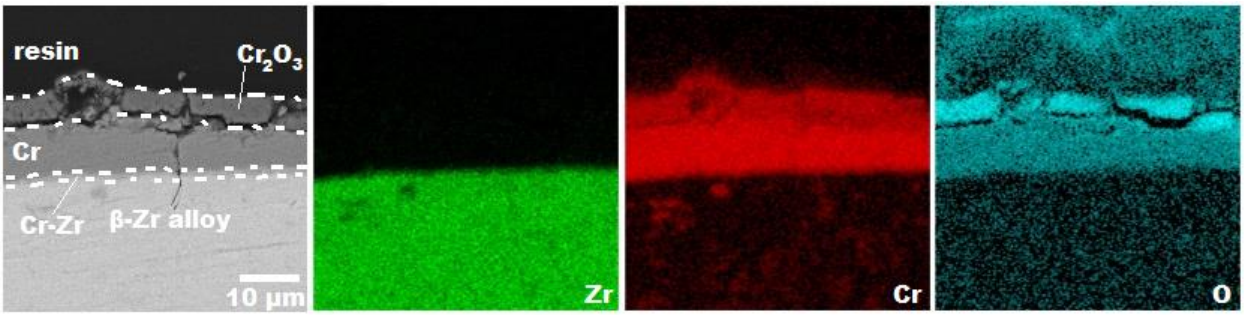


**Figure 6.** Cross-section SEM image of the Cr-coated LBW E110 alloy sample after 45 min oxidation and corresponding EDS maps of Zr, Cr, and O.

## 4. Discussion

Chromium coatings deposited by magnetron sputtering significantly improve the oxidation resistance of zirconium alloy laser beam welds at 1100 °C in an air atmosphere. The uncoated LBW alloy demonstrated linear oxidation kinetics and strongly oxidized even after 2 min which well correlates with previous studies [26,27]. The oxidation kinetics of Cr-coated LBW samples had a close to parabolic law up to 60 min that is caused by the growth of dense protective chromia scale. The sample oxidized for 90 min also had a protective oxide scale, but its weight gain did not correspond to the parabolic law due to the detrimental oxidation of the uncoated area. Thus, the outer protective scale can decrease the diffusion of oxygen and nitrogen into the LBW E110 alloy at 1100 °C in an air atmosphere for at least 90 min.

Despite the protective Cr coating, the microstructure of the Cr-coated LBW alloy changed in all zones after high-temperature oxidation. Before oxidation, a Widmanstetten microstructure consisting of interlaced α-Zr plates in primary β-Zr grains was observed only in WZ and HAZ. However, a similar microstructure was found in all zones in the oxidized samples which are caused by the β→α transition of Zr alloy during the cooling stage of oxidation tests. The samples oxidized for 2–30 min had the same thickness (2–4 μm) of α-Zr plates, while the increase in α plate thickness was observed at a longer oxidation period. The growth of α-Zr plates thickness is initiated by the diffusion of oxygen through the protective Cr coating to the LBW alloy. According to the Zr-O phase diagram [33], a β-Zr phase has a low solubility limit of oxygen at 1100 °C (<3 at.%). Therefore, the oxygen stabilized α-Zr(O) phase with a higher solubility limit (~29.5 at.%) is formed. The increase in thickness of α-Zr(O) plates up to 20 μm is found after oxidation for 90 min.

The changes in microstructure led to the corresponding hardening of LBW samples. Oxidation of uncoated LBW samples even during a short period (2 min) resulted in a strong increase in hardness due to the forming of thick $ZrO_2$ layers. At higher oxidation time (10 min), there was no possibility to measure the hardness of the uncoated LBW sample because of their fracture. It is well observed that the hardness in all regions did not change up to 30 min of oxidation for Cr-coated LBW samples. At longer oxidation, the increase in hardness occurred due to the formation of hard α-Zr(O) plates with higher thicknesses. According to Figure 4, the hardness increased from 220, 230, and 200 to 370, 350, and 315 HV after 90 min oxidation for WZ, HAZ, and bulk zones of LBW alloy, respectively. The bending test also demonstrated different mechanical behavior of the oxidized LBW samples. Before oxidation, the LBW sample had a deformation behavior typical for ductile materials. The analysis of the load-displacement curves showed brittle fracture behavior of the uncoated sample even after oxidation for 2 min (Figure 5). This sample failed in WZ at the load of 0.77 kgf, which can be seen in the cross-section SEM image. The Cr-coated samples demonstrated plastic deformation behavior in the same displacement range as for the initial LBW alloy. However, the slope of deformation curves in the elastic strain region became higher as the oxidation time increased, indicating an increase in the elastic modulus of the LBW alloy. The deformation of oxidized samples led to the formation of

cracks at $Cr_2O_3$/Cr and Cr/Zr interfaces and their propagation into the residual Cr layer and Zr alloy.

In summary, the 14.4 μm-thick Cr coating can prevent the formation of $ZrO_2$ in LBW E110 alloy up to 90 min at 1100 °C in an air atmosphere. However, the diffusion of oxygen and growth of brittle α-Zr(O) plates inside the welded Zr alloy can change the mechanical behavior of the Cr-coated LBW alloy which should be taken into account for the evaluation of its oxidation resistance under accidental conditions.

## 5. Conclusions

Chromium coating deposition by magnetron sputtering was applied to improve oxidation resistance of laser beam welds produced from E110 zirconium alloy. Due to the growth of the outer protective chromia scale, the oxidation kinetics of the Cr-coated LBW Zr alloy demonstrated the parabolic law, which is typically observed for diffusion-controlled oxidation of metals. Nevertheless, changes in cross-section microstructure due to the stabilization of hard and brittle α-Zr(O) plates in primary β-Zr grains can cause hardening of the welded Zr alloy and an increase in its elastic modulus. Despite this, Cr coating deposition should be more beneficial for welded Zr alloy as a brittle fracture deformation of the uncoated one was found even in the case of high-temperature oxidation for 2 min.

**Author Contributions:** Conceptualization, E.B.K. and D.V.S.; Methodology, D.V.S.; Validation, E.B.K.; Formal analysis, E.B.K. and D.V.S.; Investigation, K.S.G., D.A.A. and A.V.A.; Resources, D.V.S. and E.B.K.; Data curation, D.A.A.; Writing—original draft preparation, K.S.G. and D.A.A.; Writing—review and editing, E.B.K. and D.V.S.; Visualization, K.S.G. and D.A.A.; Supervision, D.V.S.; Project administration, D.V.S.; Funding acquisition, E.B.K. and D.V.S. All authors have read and agreed to the published version of the manuscript.

**Funding:** The work was supported by the Russian Science Foundation [grant No. 19-79-10116].

**Institutional Review Board Statement:** Not applicable.

**Informed Consent Statement:** Not applicable.

**Data Availability Statement:** Not applicable.

**Acknowledgments:** This research was supported by a TPU development program.

**Conflicts of Interest:** The authors declare no conflict of interest.

## References

1. Duan, Z.; Yang, H.; Satoh, Y.; Murakami, K.; Kano, S.; Zhao, Z.; Shen, J.; Abe, H. Current status of materials development of nuclear fuel cladding tubes for light water reactors. *Nucl. Eng. Des.* **2017**, *316*, 131–150. [CrossRef]
2. Kim, C.; Tang, C.; Grosse, M.; Maeng, Y.; Jang, C.; Steinbrueck, M. Oxidation mechanism and kinetics of nuclear-grade FeCrAl alloys in the temperature range of 500–1500 °C in steam. *J. Nucl. Mater.* **2022**, *564*, 153696. [CrossRef]
3. Doyle, P.; Sun, K.; Snead, L.; Katoh, Y.; Bartels, D.; Zinkle, S.; Raiman, S. The effects of neutron and ionizing irradiation on the aqueous corrosion of SiC. *J. Nucl. Mater.* **2020**, *536*, 152190. [CrossRef]
4. Steinbrueck, M.; Grosse, M.; Stegmaier, U.; Braun, J.; Lorrette, C. Oxidation of silicon carbide composites for nuclear applications at very high temperatures in steam. *Coatings* **2022**, *12*, 875. [CrossRef]
5. Yang, J.; Wu, X.; Wu, L.; Zhong, Y.; Xin, H.; Chen, Q.; Zhang, W.; Yang, J.; Zhu, C.; Ning, Z.; et al. Microstructure, mechanical properties and corrosion behavior of $Al_x$CrMoNbZr multiprincipal element alloy coatings for accident-tolerant fuel claddings: Effect of Al content. *Surf. Coat. Technol.* **2022**, *444*, 128656. [CrossRef]
6. Shen, S.; Wu, Z.; Wang, Y.; Xu, C.; Xu, J.; Wu, J.; Yan, Y.; Liu, P.; Wang, H.; Fu, E. Microstructure and radiation stability of nano-dispersoids in particle-reinforced FeCrAl alloys with different Zr concentrations. *J. Alloys Compd.* **2022**, *925*, 166625. [CrossRef]
7. Sartowska, B.; Starosta, W.; Waliś, L.; Smolik, J.; Pańczyk, E. Multi-elemental coatings on zirconium alloy for corrosion resistance improvement. *Coatings* **2022**, *12*, 1112. [CrossRef]
8. Yook, H.; Lee, Y. Post-LOCA ductility assessment of Zr-Nb Alloy from 1100 to 1300 °C to explore variable peak cladding temperature and equivalent cladding reacted safety criteria. *J. Nucl. Mater.* **2022**, *567*, 153829. [CrossRef]
9. Le Saux, M.; Brachet, J.C.; Vandenberghe, V.; Ambard, A.; Chosson, R. Breakaway oxidation of zirconium alloys exposed to steam around 1000 °C. *Corros. Sci.* **2020**, *176*, 108936. [CrossRef]

10. Brachet, J.C.; Le Saux, M.; Bischoff, J.; Palancher, H.; Chosson, R.; Pouillier, E.; Guilbert, T.; Urvoy, S.; Nony, G.; Vandenberghe, T.; et al. Evaluation of equivalent cladding reacted parameters of Cr-coated claddings oxidized in steam at 1200 °C in relation with oxygen diffusion/partitioning and post-quench ductility. *J. Nucl. Mater.* **2020**, *533*, 152106. [CrossRef]
11. Brachet, J.C.; Rouesne, E.; Ribis, J.; Guilbert, T.; Urvoy, S.; Nony, G.; Toffolon-Masclet, C.; Le Saux, M.; Chaabane, N.; Palancher, H.; et al. High temperature steam oxidation of chromium-coated zirconium-based alloys: Kinetics and process. *Corros. Sci.* **2020**, *167*, 108537. [CrossRef]
12. Kashkarov, E.; Afornu, B.; Sidelev, D.; Krinitcyn, M.; Gouws, V.; Lider, A. Recent advances in protective coatings for accident tolerant Zr-based fuel claddings. *Coatings* **2021**, *11*, 557. [CrossRef]
13. Yang, J.; Steinbrück, M.; Tang, C.; Große, M.; Liu, J.; Zhang, J.; Yun, D.; Wang, S. Review on chromium coated zirconium alloy accident tolerant fuel cladding. *J. Alloys Compd.* **2022**, *895*, 162450. [CrossRef]
14. Slobodyan, M. Resistance, electron- and laser-beam welding of zirconium alloys for nuclear applications: A review. *Nucl. Eng. Technol.* **2021**, *53*, 1049–1078. [CrossRef]
15. Tao, W.; Cai, C.; Li, L.; Chen, Y.; Ling Wang, Y. Pulsed laser spot welding of intersection points for Zircaloy-4 spacer grid assembly. *Mater. Des.* **2013**, *52*, 487–494. [CrossRef]
16. Cai, C.; Li, L.; Tao, W.; Peng, G.; Wang, X. Weld bead size, microstructure and corrosion behavior of zirconium alloys joints welded by pulsed laser spot welding. *J. Mater. Eng. Perform.* **2016**, *25*, 3783–3792. [CrossRef]
17. Elkin, M.; Kiselev, A.; Slobodyan, M. Pulsed laser welding of Zr1%Nb alloy. *Nucl. Eng. Technol.* **2019**, *51*, 776–783. [CrossRef]
18. Lupakov, I.; Rodchenkov, B.; Vukolova, V.; Tyurin, V. Structure and phase composition of weldments in the Zr−2.5Nb alloy. *Met. Sci. Heat. Treat.* **1973**, *15*, 379–381. [CrossRef]
19. Blackburn, J. 3—Laser Welding of Metals for Aerospace and Other Applications. In *Welding and Joining of Aerospace Materials*; Chaturvedi, M.C., Ed.; Woodhead Publishing: Cambridge, UK, 2012; pp. 75–108.
20. Vandegrift, J.; Parga, C.J.; Coryell, B.; Butt, D.P.; Jaques, B.J. Oxidation behavior of welded Zry-3, Zry-4, and Zr–1Nb tubes. *Nucl. Mater. Energy* **2019**, *21*, 100714. [CrossRef]
21. Jeong, Y.H.; Kim, H.G.; Kim, T.H. Effect of β phase, precipitate and Nb-concentration in matrix on corrosion and oxide characteristics of Zr–xNb alloys. *J. Nucl. Mater.* **2003**, *317*, 1–12. [CrossRef]
22. Sidelev, D.; Ruchkin, S.; Kashkarov, E. High-temperature oxidation of Cr-coated resistance upset welds made from E110 alloy. *Coatings* **2021**, *11*, 577. [CrossRef]
23. Sidelev, D.; Kashkarov, E.; Grudinin, V.; Krinitcyn, M. High-temperature oxidation of Cr-coated laser beam welds made from E110 zirconium alloy. *Corros. Sci.* **2022**, *195*, 110018. [CrossRef]
24. Sidelev, D.V.; Kashkarov, E.B.; Syrtanov, M.S.; Krivobokov, V.P. Nickel-chromium (Ni–Cr) coatings deposited by magnetron sputtering for accident tolerant nuclear fuel claddings. *Surf. Coat. Technol.* **2019**, *369*, 69–78. [CrossRef]
25. Sidelev, D.V.; Poltronieri, C.; Bestetti, M.; Krinitcyn, M.G.; Grudinin, V.A.; Kashkarov, E.B. A comparative study on high-temperature air oxidation of Cr-coated E110 zirconium alloy deposited by magnetron sputtering and electroplating. *Surf. Coat. Technol.* **2022**, *433*, 128134. [CrossRef]
26. Steinbrück, M. Prototypical experiments relating to air oxidation of Zircaloy-4 at high temperatures. *J. Nucl. Mater.* **2009**, *392*, 531–544. [CrossRef]
27. Steinbrück, M.; Oliveira da Silva, F.; Grosse, M. Oxidation of Zircaloy-4 in steam-nitrogen mixtures at 600–1200 °C. *J. Nucl. Mater.* **2017**, *490*, 226–237. [CrossRef]
28. Caplan, D.; Sproule, G.I. Effect of oxide grain structure on the high-temperature oxidation of Cr. *Oxid. Met.* **1975**, *9*, 459–472. [CrossRef]
29. Kashkarov, E.B.; Sidelev, D.V.; Syrtanov, M.S.; Tang, C.; Steinbrück, M. Oxidation kinetics of Cr-coated zirconium alloy: Effect of coating thickness and microstructure. *Corros. Sci.* **2020**, *175*, 108883. [CrossRef]
30. Druffel, T.; Buazza, O.; Lattis, M.; Farmer, S.; Spencer, M.; Mandzy, N.; Grulke, E.A. The role of nanoparticles in visible transparent nanocomposites. *J. Int. Soc. Opt. Eng.* **2008**, *7030*, 70300. [CrossRef]
31. Jiang, J.; Du, M.; Pan, Z.; Yuan, M.; Ma, X.; Wang, B. Effects of oxidation and inter-diffusion on the fracture mechanisms of Cr-coated Zry-4 alloys: An in situ three-point bending study. *Mater. Des.* **2021**, *212*, 110168. [CrossRef]
32. Jiang, J.; Du, M.; Ma, X. On the microstructures and cracking modes of Cr-coated Zr-4 alloys oxidized and vacuum-annealed at 1000 °C. *J. Alloys Compd.* **2022**, *908*, 1646110. [CrossRef]
33. Wang, C.; Zinkevich, M.; Aldinger, F. On the thermodynamic modeling of the Zr-O system. *J. Calphad* **2004**, *28*, 281–292. [CrossRef]